




Cite this: *Phys. Chem. Chem. Phys.*, 2023, 25, 7994

Rational design of non-fullerene acceptors via side-chain and terminal group engineering: a computational study†

Rudranarayan Khatua,‡ Bibhas Das‡ and Anirban Mondal *

We investigated the optoelectronic and photovoltaic properties of three types of acceptor–donor–acceptor-based non-fullerene acceptor (NFA) molecules for organic solar cell (OSC) applications. Density functional theory and its time-dependent variant were employed to compute the quadrupole moment perpendicular to the π -system (Q_{20}), open circuit voltage (V_{OC}), and other relevant solar cell parameters. The role of functionalization in the acceptor unit on the overall device performance was explored by incorporating halogen and methoxy-based electron-withdrawing groups. The electronegativity differences between the halogen atoms and the methoxy group demonstrated contrasting effects on the energy levels, molecular orbitals, and absorption maximum. We observed a trade-off between short-circuit current (J_{SC}) and V_{OC} , which was further substantiated by an inverse correlation between Q_{20} and V_{OC} . We found an optimum value of Q_{20} in the range of 80 to 130 ea_0^2 to achieve an optimized solar cell performance. Among the designed systems, Se-derived NFAs with a small band gap, red-shifted absorption maximum, high-oscillator strength, small exciton binding energy, and optimum Q_{20} turned out to be potential candidates for future applications. These criteria can be generalized to design and screen next-generation non-fullerene acceptors to achieve improved OSC performance.

Received 21st December 2022,
 Accepted 7th February 2023

DOI: 10.1039/d2cp05958d

rsc.li/pccp

1. Introduction

In recent years, the power conversion efficiencies (PCEs) of organic solar cells (OSCs) have dramatically increased owing to the emergence of a new class of strongly absorbing dyes to replace the fullerene acceptors.^{1,2} At present, OSCs comprising small molecule non-fullerene acceptors (NFAs), blended with donor polymers, offer PCEs up to 18%,^{3–6} while fullerene-based OSCs are only 10% efficient.⁷ The significant advantages of NFAs over their fullerene-based counterparts are the large open-circuit voltage, wide absorption ranges, and high short circuit current density, which are accountable for enhancing the PCEs.^{8–13} However, the PCEs of conventional solar devices, such as perovskites and c-Si cells, are still superior to that of the state-of-the-art OSCs.¹⁴ The loss of efficiency in the latter case can be attributed to energy losses during the conversion of a photon to free charge carriers.^{15,16} Therefore, novel small

molecule NFAs with inherently low loss of energy are highly desired to improve the photovoltaic performance of OSCs further and subsequently address the challenge for large-scale commercialization of OSCs.

The successful molecular architecture for the NFAs has been a fused acceptor–donor–acceptor (A–D–A) type, which has been established as an efficient strategy for enhancing the performance of OSCs. The essential components in the A–D–A-based architecture include a ladder-type electron donor core, electron-withdrawing terminal groups acting as acceptors, and alkyl side chains that assist solubility and govern molecular packing.^{17,18} Therefore, careful modifications of each component and their different combinations allow us to adjust the energy levels, absorption from visible to NIR regions, mobility, solubility, and electronic properties of the NFA molecules.^{19–24} Bin *et al.*²⁵ and Qian *et al.*²⁶ have achieved remarkable external quantum efficiencies in OSCs based on NFAs by tuning the energy offsets of ionization potential (IP) and electron affinity (EA) between donors and acceptors to a minimum. Laquai and coworkers have demonstrated the role of bulk IP offsets, typically larger than 0.5 eV, to obtain the efficient barrierless conversion of the charge transfer state to free charge and high internal quantum efficiencies.²⁷ More recently, it was shown that the acceptor's quadrupole moment significantly impacts the interfacial energetics, charge generation, and recombination process in NFA-

Discipline of Chemistry, Indian Institute of Technology Gandhinagar, Gujarat, 382355, India. E-mail: amondal@iitgn.ac.in

† Electronic supplementary information (ESI) available: Chemical structures of donor polymers, iso-electrostatic potential surfaces, frontier molecular orbitals, total and partial density of states, absorption spectra, transition density matrix, energy levels, torsional angles, dipole moment, open-circuit voltage, short-circuit current, and fill-factor. See DOI: <https://doi.org/10.1039/d2cp05958d>

‡ These authors contributed equally to this work.

based donor-acceptor blends.^{28,29} In addition, end group engineering is a popular approach to enhance the charge transport in NFA molecules, as already highlighted in literature reports.^{30–35} The impact of fluorination in the terminal acceptor unit was demonstrated as one of the valuable strategies to lower the molecular orbital energy levels and shift the absorption maximum towards the near-infrared region, leading to an overall improvement in the performance of the organic solar cells.^{31,36,37}

Despite these studies, the selection, design, and fabrication of NFAs for high-performing OSCs still pose significant challenges due to the lack of precise insight into the structure–property interplay, which prevents guided (*i.e.*, computer-aided or *in-silico*) material design. Although several computational and theoretical studies are available in fullerene-based acceptors, detailing the importance of critical parameters in governing charge transport, such as energetic disorder and reorganization energy, computational investigations on NFAs are limited.^{38–42} Employing the first-principle framework, Liu *et al.* examined exciton diffusion in a fused-ring electron acceptor, indaceno-dithiophene (IDT) endcapped with 1,1-dicyanomethylene-3-indanone (IDIC).⁴³ Zhang *et al.* performed combined density functional theory (DFT) and molecular dynamics (MD) simulations to reveal the presence of distinctive π – π molecular packing in the thin films of Y6 NFA.⁴⁴ They described the effect of such molecular packing in the delocalization of electron wavefunctions at donor/acceptor interfaces that leads to a significant reduction in the Coulomb attraction between interfacial electron–hole pairs. The role of fluorination and π -extension in the mobility and intermolecular π – π stacking between end groups in the 3,9-bis(2-methylene-(3-(1,1-dicyanomethylene)-indanone)-5,5,11,11-tetrakis(4-hexylphenyl)-dithieno[2,3-*d*:2',3'-*d'*]-s-indaceno[1,2-*b*:5,6-*b'*]-dithiophene) (ITIC) acceptor was reported by Han *et al.*^{45,46} Yang *et al.* investigated the electronic, optical, and interfacial charge-transfer properties in a series of end-capped manipulated functionalized Y6 NFAs using DFT, time-dependent DFT (TD-DFT), and MD simulations.⁴⁷ They observed significant improvement in electron mobility, more than 20 times that of the parent molecule due to functionalization. Using multiscale techniques, Yao *et al.* designed environmentally friendly fused-ring electron acceptors by replacing the toxic cyano group with $-\text{CF}_3$, $-\text{SO}_3\text{H}$, and $-\text{NO}_2$.⁴⁸ Y6-based asymmetric A–D1AD2–A type NFAs were designed by Li and co-workers employing quantum chemical calculations.⁴⁹ These studies provided insight into the impact of the energetic landscape on the overall OSC performance and enhanced the understanding of the structure–property relationship in NFAs. Despite this, a window exists for further improvement of the power conversion efficiency with high open circuit voltage and broad absorption spectrum for efficient organic solar cells.

Herein we present a computational study on fifteen NFA molecules' photovoltaic and optoelectronic properties. The selection and design of the NFAs are significant challenges for achieving better photovoltaic and optoelectronic materials for solar cell applications. We choose a sizable representative from the experimentally reported compounds to analyze the photovoltaic characteristics and optoelectronic properties.

As reported, these materials' PCE and short circuit current (J_{sc}) cover broad ranges, 5.8–13.1% and 12.31–20.88 mA cm^{-2} , respectively. In addition, we have designed seven new NFAs by end-group modifications while controlling the positions of the halide atoms (F and Cl) and $-\text{OMe}$ groups in the acceptor moieties. The presence of electronegative groups can alter the positions of the molecular orbitals and, thus, the device's open-circuit voltage (V_{oc}). Furthermore, selenium-based designed NFAs are formed by eliminating the vinyl linker so that the donor and acceptor can bind directly in a single covalent bond. Substitution of Sulfur by Selenium and the direct linking between donor and acceptor groups *via* a double bond extends the conjugation and yields a better intramolecular charge transfer and, subsequently, a red-shifted absorption. Overall, our strategy is to explore the effect of these substitutions on the intra-molecular interactions and photovoltaic performances to open new possibilities for developing efficient acceptors for OSCs.

2. Computational details

All quantum chemical calculations were performed at the density functional theory (DFT) level using the Gaussian 09 program suite.⁵⁰ Initial configurations were constructed using the GaussView software.⁵¹ The B3LYP functional⁵² in conjunction with the 6-31G(d,p) basis set was employed to carry out ground state geometry optimizations of the NFA systems. Optimized minima on the potential energy surface were confirmed *via* frequency analysis. Previous literature reports showed that the predicted fundamental energy gap using the B3LYP/6-31G(d,p) method was close to the experimentally measured values for a set of NFA compounds.⁵³ Therefore, we chose this method to perform all the structural optimizations for the designed acceptor molecules. To obtain a better estimate of the energy levels, single-point calculations were carried out on the optimized geometries using the B3LYP/6-31+G(d,p) level of theory. The energies of the frontier molecular orbitals, $E_{\text{HOMO}}-E_{\text{LUMO}}$, and reorganization energies⁵⁴ are obtained at the same level of theory. Molecular quadrupole moment was derived using the GDMA program.⁵⁵ The input (density matrix) for the GDMA calculations comes from the gas-phase computations described above.

For the description of excited states, we employed linear-response time-dependent density functional theory (TD-DFT)⁵⁶ to compute the excitation energies, absorption maximum (λ_{max}), and oscillator strengths (f). TD-DFT calculations were performed considering chloroform (CHCl_3 , $\epsilon = 4.7113$) as the solvent using the polarizable conductor calculation model (CPCM).⁵⁷ For these calculations, we tested a few DFT methods such as B3LYP, CAM-B3LYP, and ω B97XD in combination with 6-31+G(d,p) basis sets against experimentally available data. For example, the maximum absorption wavelength of IT-F at the B3LYP/6-31+G(d,p) level (720 nm) agreed well with the experimental result (717 nm) as compared to other methods such as CAM-B3LYP/6-31+G(d,p) (577 nm) and ω B97XD/6-31+G(d,p) (545 nm). A detailed comparison of the absorption

Table 1 Computed absorption wavelength (λ_{max}), excitation energy (E_x), oscillator strength (f), and exciton binding energy (E_b) of NFA molecules at the TD-DFT/B3LYP/6-31+G(d,p) level in CHCl_3 solvent using a CPCM model. Experimental λ_{max} values are given in parentheses

Compounds	E_x (eV)	λ_{max} (nm)	f	E_b (eV)
IT-H	1.749	709 (700) ⁶²	2.801	0.349
IT-F	1.722	720 (717) ⁶²	2.722	0.345
IT-Cl	1.699	730	2.883	0.350
ITIC-Th	1.760	704 (668) ⁶³	2.703	0.341
ITIC-Th-1	1.768	701	2.651	0.349
ITIC-Th-2	1.726	718	2.634	0.336
ITIC-Th-3	1.760	704 (500–750) ⁶³	2.729	0.340
ITIC-Th-4	1.736	714	2.636	0.332
IT-OMe-1	1.814	683 (650) ⁶⁴	2.817	0.363
IT-OMe-2	1.727	718 (678) ⁶⁴	2.836	0.353
IT-OMe-3	1.778	697 (664) ⁶⁴	2.973	0.358
IT-OMe-4	1.751	708 (676) ⁶⁴	2.710	0.351
SeTIC	1.170	1060	3.148	0.145
SeTIC-F	1.165	1064	3.141	0.116
SeTIC-Cl	1.133	1093	3.231	0.140

maximum between experimental measurements and predicted values is provided in Table 1. We observed the B3LYP/6-31+G(d,p) combination to be the most suitable since it exhibited the best agreement with the experimental results. Thus, it was considered for all future TD-DFT calculations.

The device performance of solar cells represented by the power conversion efficiency (PCE) depends mainly on three factors, open-circuit voltage (V_{OC}), fill factor (FF), and short circuit current (J_{SC}), as illustrated through eqn (1).

$$\text{PCE} = \frac{J_{\text{SC}} V_{\text{OC}} \text{FF}}{P_{\text{in}}} \quad (1)$$

Here, P_{in} is the power of the incident light that falls on the device's surface. V_{OC} is an essential parameter for organic solar cell fabrication. At zero current, V_{OC} represents the maximum voltage drawn out of the cell during operation.⁵⁸ It highlights the maximum working ability of OSCs. V_{OC} values are calculated theoretically using eqn (2).⁵⁹

$$V_{\text{OC}} = (|E_{\text{HOMO}}^{\text{D}}| - |E_{\text{LUMO}}^{\text{A}}|) - 0.3 \quad (2)$$

Here $E_{\text{HOMO}}^{\text{D}}$ and $E_{\text{LUMO}}^{\text{A}}$ are the HOMO and LUMO energy levels of the donor and NFA molecules, respectively. In order to obtain V_{OC} values, we have considered four donor molecules, as shown in Fig. S1 of the (ESI[†]). The geometries and energies of the donor molecules are computed at the same level of theory as described for the NFA molecules.

The Multiwfn 3.7 program⁶⁰ was used for the transition density matrix (TDM) analysis that helped to understand the electronic excitation processes. VMD⁶¹ was used to generate the 3D surface plots.

3. Results and discussion

Gas-phase structure

The chemical structures of the investigated NFAs are displayed in Fig. 1. One of our goals is to examine the effect of the functional group modification on the π -conjugated backbone

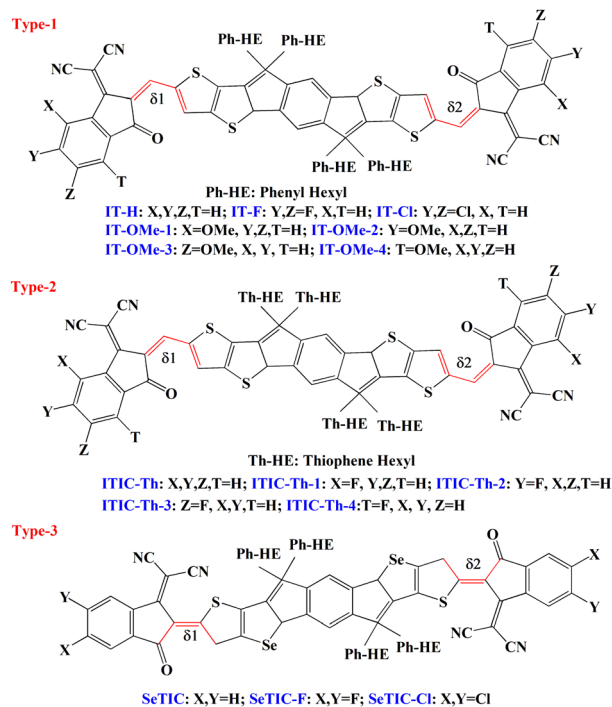


Fig. 1 Chemical structures of the investigated non-fullerene acceptor (NFA) molecules in the present work.

and, subsequently, the degree of overlap in the frontier molecular orbitals that affect the overall OSC performance. Towards this, several functional moieties were considered, such as halogen atoms ($-\text{F}$, $-\text{Cl}$), methoxy ($-\text{OMe}$), phenyl hexyl (Ph-HE), and thiophene hexyl (Th-HE). Depending upon the peripheral and end group modifications, the studied NFA systems can be grouped into three types. Type-1 systems consist of phenyl hexyl linked donors and are either methoxy or halogen-substituted at the terminal position (IT-H, IT-F, IT-Cl, IT-OMe-1, IT-OMe-2, IT-OMe-3, and IT-OMe-4). On the other hand, Type-2 systems are fluorine substituted at the end position with thiophene hexyl moieties present in the peripheral part (ITIC-Th, ITIC-Th-1, ITIC-Th-2, ITIC-Th-3, and ITIC-Th-4). Type-3 NFAs are designed with Se atoms in the core with a phenyl hexyl group present as the side chain, and the terminal part consists of either fluorine or chlorine atoms (SeTIC, SeTIC-F, and SeTIC-Cl). The topology of the investigated NFAs is analyzed based on the two torsional angles connecting the donor and acceptor units in an NFA molecule, δ_1 and δ_2 , as defined in Fig. 1. Among the Type-1 and Type-2 systems, all the NFAs are found to be planar with the values of the torsional angles close to ~ 0 (see Table S1 of the ESI[†]). Exceptions to these are IT-OMe-1 and ITIC-Th-1, which have slightly larger dihedral angles of $4.281^\circ/4.579^\circ$ (δ_1/δ_2) and $5.535^\circ/5.537^\circ$ (δ_1/δ_2), respectively. This is due to the steric effects of the $-\text{F}$ or $-\text{OMe}$ group incorporated much nearer to the $-\text{CN}$ group in the acceptor moieties, which makes the molecule slightly twisted. Furthermore, all Type-3 systems exhibit a nonplanar geometry with almost similar twisting angle values for δ_1 and δ_2 around 16.84° , 16.985° , and 17.112° , respectively. This observation indicates that the absence of a vinyl linker between the donor and acceptor units

in the SeTIC derivatives induces a significant change in the overall geometry. As a consequence, Type-3 systems possess more prominent dipole moments as compared to Type-1 or Type-2 NFAs. Based on these preliminary observations, we anticipate that the peripheral and end-group modification in the donor and acceptor parts may influence the photovoltaic parameters of the investigated NFAs.

Molecular electrostatic potential

The electrostatic potential (ESP) maps of the IT-OMe-based compounds are displayed in Fig. 2. Similar surface plots of the remaining systems are shown in Fig. S2 of the ESI.† It is evident from Fig. 2 that the positive part of the ESP (green color mapped region) is distributed over the entire π -conjugated system, except for the -CN, -OMe, and -O atoms, which are more electron-withdrawing in nature. The negative ESP (mauve color mapped region) is located more on electron-withdrawing groups. It is shifted towards the -OMe group as its position is altered from ortho to meta to para in the IT-OMe derivatives. A similar trend can also be observed in the ITIC-Th derivatives (Fig. S2 of the ESI†) by simply altering the position of the -F atom in peripheral positions (X, Y, Z, and T) of the acceptor unit. In the SeTIC and IT-H derivatives, we observed negative ESP on the halogen atoms, whereas other atoms in the π -conjugated system are assigned to positive ESP.

Energy levels

Ionization potential (IP), electron affinity (EA), and reorganization energy (λ) are essential parameters for accurately describing charge transport in NFA systems. The following equations estimate IP and EA. $IP = E^{cC} - E^{nN}$, where E^{cC} is the energy of the cation calculated from the optimized geometry of the cation, and E^{nN} is the energy of the neutral molecule calculated from the optimized neutral geometry. $EA = E^{nN} - E^{aA}$, where E^{aA} is the energy of the anion calculated from the optimized geometry of the anion. The computed IP, EA, and λ for holes

and electrons are summarized in Table S1 of the ESI.† Compared to their parent compound, IT-H or SeTIC, the halogen-substituted derivatives exhibit a net increase (0.15 to 0.2 eV) in the IP value. The corresponding increase in the EA values is around 0.2 to 0.23 eV. However, the introduction of -OMe groups in the terminal position of the acceptor units has an opposite effect compared to their halogen counterparts. The IP and EA values in -OMe substituted Type-1 compounds are reduced by 0.11 to 0.17 eV and 0.08 to 0.21 eV, respectively. Such contrasting development can be attributed to the difference in electron-withdrawing abilities between the halogen and -OMe groups. Interestingly, in the Type-2 systems, incorporating a single -F atom in the acceptor units has a minor impact on the IP and EA values. Although the trend is similar to Type-1 and Type-3 compounds, the magnitude is less than or equal to 0.1 eV. A lesser influence can be rationalized based on the number of halogen substitutions made in Type-2 NFAs (one on each acceptor unit) compared to Type-1 or Type-3 systems (two on each acceptor unit).

On the other hand, a system's reorganization energy accounts for the charging and discharging of a molecule. During charge hopping from a molecule, i to molecule j , the reorganization energy is a sum of the internal contribution due to the internal reorganization of the two molecules and an external contribution due to the relaxation of the surroundings.⁵⁴ The internal reorganization energy is calculated as $\lambda_{ij} = (E_i^{nC} - E_i^{nN}) + (E_j^{cN} - E_j^{cC})$, for molecule i and j , where the lowercase represents the neutral (n) or charged (c) molecule and the uppercase represents the neutral (N) or charged (C) geometry. In the current framework, the external contribution to the reorganization energy is ignored since in the amorphous organic semiconductors (*e.g.*, NFAs), the Pekar factor is on the order of 0.01,⁵⁴ leading to a relatively small contribution to the total reorganization energy. In general, larger reorganization energy indicates a poorer transport of charge carriers. As evident from Table S1 of the ESI,† in the SeTIC derivatives, a significant difference is observed between λ_h (~ 0.13 eV) and λ_e (~ 0.32 eV). The reorganization energy for electrons is more than twice that for the holes, indicating that these systems would have much smaller electron mobility than holes. Such large λ_e can be explained based on the significantly distorted structures of Type-3 compounds in their anionic form ($\delta 1/\delta 2$ in the range around ~ 23). In contrast, the λ values for both holes and electrons are comparable in Type-2 NFAs. In the case of Type-1 compounds, λ_e is slightly smaller than λ_h , with the only exception being IT-OMe-1.

Frontier molecular orbitals

The distribution of the frontier molecular orbitals, HOMO and LUMO, plays a critical role in governing the intra-molecular charge transfer in NFAs. Fig. 3 displays the HOMO and LUMO distributions in a few selected NFA systems, whereas, for the remaining compounds, it is shown in Fig. S3 of the ESI.† The individual energy levels and HOMO-LUMO (H-L) gap of the investigated NFAs are tabulated in Table S1 of the ESI.† As depicted in Fig. 3 and Fig. S3 of the ESI,† both the HOMO and LUMO are primarily distributed over the π -conjugated

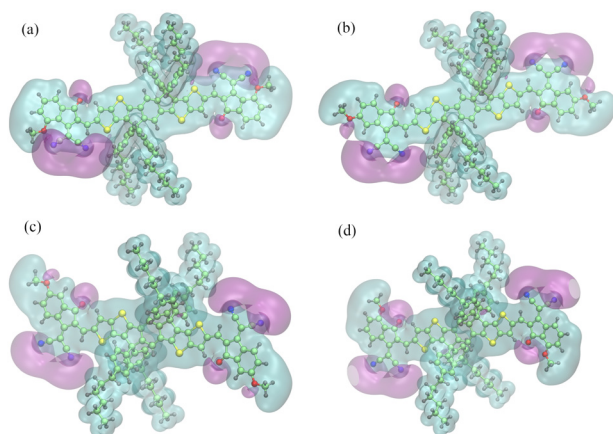


Fig. 2 Iso-electrostatic potential surfaces of selected non-fullerene acceptors: (a) IT-OMe-1, (b) IT-OMe-2, (c) IT-OMe-3, and (d) IT-OMe-4. Similar surface plots for the remaining systems are shown in Fig. S2 of the ESI.†

units in the studied NFAs. In general, the peripheral alkyl linker shares a small share of the HOMO, whereas the LUMO concentrates more on the acceptor part of the NFAs. However, in the SeTIC derivatives, we observe an electronic cloud of HOMO and LUMO distributed almost equally over the donor and acceptor units due to the sizeable intra-molecular interaction in the presence of the Se atom in the system. Both halogen and methoxy substitution tend to enhance the delocalization of the electronic cloud towards the acceptor moieties, indicating the effect of the electron-withdrawing group present in the acceptor part.

On the other hand, the computed H-L gaps in the Type-1 and Type-2 systems are relatively similar, around ~ 2 eV. However, we observed a shallower band gap in the case of SeTIC derivatives, which is in the range of 1.017–1.025 eV. The low band gap may be attributed to the absence of a vinyl linker between the donor and acceptor blocks, which causes a significant enhancement of the intramolecular interactions and, eventually, reduces the band gap of the materials. We found that halogen substitution reduces the LUMO energy level compared to the parent molecule across all the investigated NFAs. In contrast, the methoxy group showed the opposite effect, leading to the potential enhancement of an OSC device's open circuit voltage, V_{OC} (see eqn (2)). We shall discuss this in the section to follow.

The total and partial density of states (DOS) computed at the B3LYP/6-31+G(d,p) level are shown in Fig. 4 and Fig. S4 of the ESI.† The DOS can further quantify the contribution of different fragments towards the frontier molecular orbital in a given NFA molecule. In Fig. 4 and Fig. S4 of the ESI,† the distribution of the total density of states is represented in a solid line, whereas donor and acceptor fragments are shown in dashed-dotted and dashed lines, respectively. The density distribution along negative x -axis values represents the valence band (HOMO), and the distribution along positive x -axis values shows the conduction band (LUMO). We observed that the distribution of electron density is located more on the donor motifs than the acceptor.

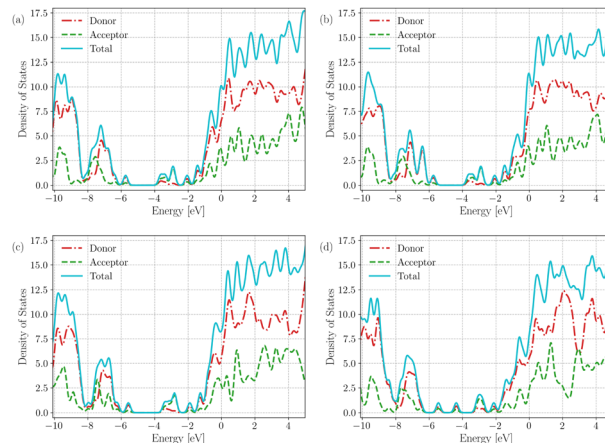


Fig. 4 The total and partial density of states (PDOS) computed at the B3LYP/6-31+G(d,p) level for the selected NFA molecules – (a) IT-H, (b) ITIC-Th, (c) IT-OMe-1, and (d) SeTIC. Similar plots for the remaining molecules are shown in Fig. S4 of the ESI.†

However, the acceptor units significantly contribute to the density of states near the Fermi level in all NFA molecules. The concentration of more partial DOS on the acceptor units around the LUMO of NFAs indicates adequate acceptor electron affinity, which can deliver improved photovoltaic properties to the OSCs. In all the studied systems, the partial DOS occupies more space around the conduction band (LUMO) compared to the valence band (HOMO), which alludes that these NFAs are potential candidates to accommodate the excited electrons efficiently. Furthermore, we noticed a slight shifting of the valence and conduction band distribution in IT-OMe-1 and IT-OMe-4 compared to IT-OMe-2 and IT-OMe-3. The –OMe group attached to the former set is nearer to the –CN and –O functional group than the latter, which may affect their electronic density distribution pattern. A similar result was obtained in ITIC-Th derivatives when we changed the likely position of the F-atom in the acceptor moieties (Fig. S4 of the ESI†). These observations point out that the substitutions of functional

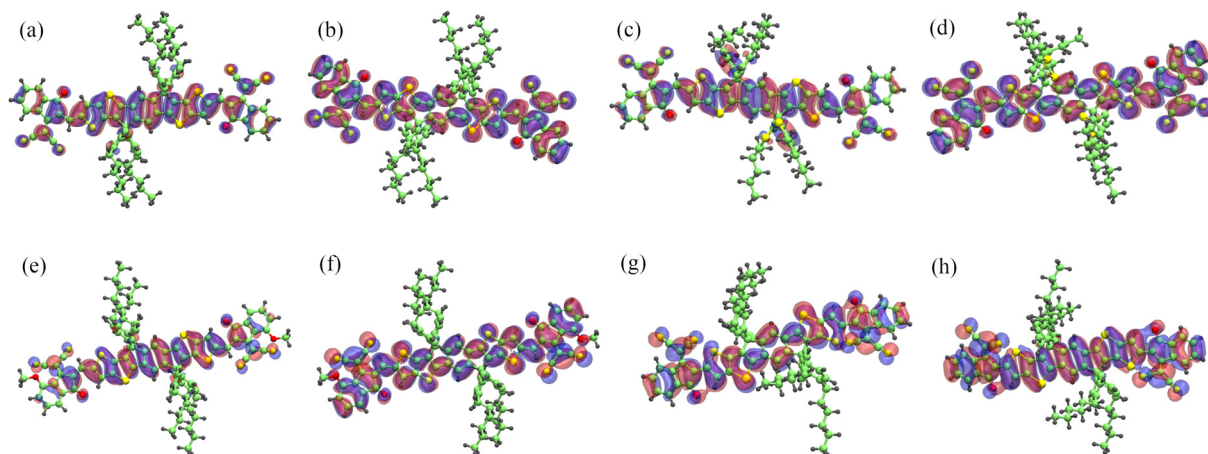


Fig. 3 Frontier molecular orbitals (HOMO and LUMO) in selected non-fullerene acceptors. HOMO: (a) IT-H, (c) ITIC-Th, (e) IT-OMe-1, and (g) SeTIC; LUMO: (b) IT-H, (d) ITIC-Th, (f) IT-OMe-1, and (h) SeTIC. Similar surface plots for the remaining systems are shown in Fig. S3 of the ESI.†

groups attached to the end-capped acceptor moieties significantly impact the electron density distribution pattern.

Photo-excitation properties

The photo-physical characteristics of the NFA systems are examined at the TD-DFT/B3LYP/6-31+G(d,p) level of theory (CPCM), considering chloroform as the solvent. These calculations involved a maximum number of 20 excited states. Fig. S5 of the ESI† displays the computed absorption spectra of the investigated systems. The absorption wavelength (λ_{max}), excitation energy (E_x), oscillator strength (f), and exciton binding energy (E_b) of the NFA molecules are tabulated in Table 1. As it is evident from Table 1, the predicted λ_{max} values show adequate agreement with the available experimental numbers.^{62–64} Halogen functionalization in Type-1 or Type-2 NFAs results in an overall bathochromic shift in the absorption maximum. The observed shift in λ_{max} is within ~ 20 nm and can be justified based on the electron-withdrawing group's presence in the acceptor motifs. A similar trend holds for Type-3 compounds as well. However, functionalization by the –OMe group showed an opposite effect in λ_{max} as we observed a blue shift in general (except for IT-OMe-2). The wavelength corresponding to the electronic excitation from S_0 to S_1 in the Type-1 and Type-2 molecules is observed in the UV-visible region with a wavelength lower than 750 nm. In the Type-3 complexes, the λ_{max} is found to be maximum and in the near-infrared region of wavelength 1060–1093 nm. Such a sizeable bathochromic shift in λ_{max} compared to the other two types of NFAs, can be explained as the absence of the vinyl linker joining the D–A groups consisting of Se atoms and eventually yields an improved interaction between the donor and acceptor units.

Excitation energies provide helpful information on the electronic excitation from the valence band to the conduction band, where an easier excitation would require a lower value of E_x . We generally observed a smaller value of E_x than the ground state band gap (Table S1 of the ESI†) energy in all the studied complexes. The SeTIC derivatives exhibit the lowest E_x following their largest λ_{max} numbers. The computed oscillator strengths are in the range of 2.6–3.2, indicating strong light absorption abilities in these NFAs. To summarize, the extended conjugation and strong A–D–A interaction resulted in lower excitation energy, red-shifted λ_{max} , and improved light absorption capabilities, ultimately reinforcing the electron–acceptor property of the NFA molecules.

Exciton binding energy is one of the critical parameters governing an organic solar cell's overall efficiency and performance. In a bulk heterojunction OSC, photons absorbed by the donor (or acceptor) molecules produce an exciton, *i.e.*, a bound electron–hole pair on the donor (or acceptor) molecule. The exciton dissociates at the interface of the donor and acceptor molecule due to the difference in energy levels. Thus, the process of a Coulomb bound exciton to free charge carrier generation requires overcoming the exciton binding energy. As expected, a low exciton binding energy is preferred for spontaneous free charge carrier generation leading to enhanced J_{SC} . The exciton binding energies of the investigated NFAs are computed

using the following equation.⁶⁵ Table 1 summarizes the computed binding energies.

$$E_b = E_{\text{HOMO-LUMO}} - E_x \quad (3)$$

Here, $E_{\text{HOMO-LUMO}}$ is the energy difference between the HOMO and LUMO energy levels, and E_x represents the first excitation energy (S_0 to S_1). As evident from Table 1, the exciton binding energies of the examined NFAs are within 0.4 eV, smaller compared to literature-reported values observed in other OSC systems.⁶⁵ Moreover, these E_b lower than 1 eV may facilitate the more significant dissociation of excitons yielding separated charge carriers and an enhancement of current density for suitable solar cell applications. Among the three types of NFAs investigated here, SeTIC derivatives possess the lowest E_b , less than 0.15 eV, suggesting that these are potential acceptor candidates for organic solar cell applications.

Photovoltaic characteristics

The performance of bulk-heterojunction OSCs can be analyzed by evaluating the V_{OC} values for a specific donor-NFA combination.⁶⁶ We employed eqn (2) to compute V_{OC} at the B3LYP/6-31+G(d,p) level of theory, considering four different donors such as PBDB-T, PBDB-T-SF, PM6, and FTAZ. The calculated V_{OC} values are summarized in Table S2 of the ESI.† The experimentally measured numbers reported in the literature for a few NFA molecules are tabulated in Table S3 of the ESI.† Tables S2 and S3 of the ESI† show that the predicted V_{OC} values consistently overestimate the experimental measurements. However, the predicted trend in V_{OC} is the same as observed in the experiment. The V_{OC} values show an increasing order as we change the donor polymer in the series, PBDB-T-SF > PM6 > FTAZ > PBDB-T, which is in accordance with the HOMO energy levels of the examined donor molecules. Across all the NFAs, we found that halogen functionalization yields a lower value of V_{OC} compared to the parent system. It can be justified based on the lower LUMO levels of NFAs functionalized with halogen atoms. This trend confirms that the halogen substitution on the end group acceptor does not help in improving the V_{OC} in OSCs. In contrast, as expected, methoxy substitution exhibits an improved V_{OC} (Table S2 of the ESI†) due to increased LUMO energy levels in acceptor molecules. In the case of the SeTIC derivatives, we observed a significantly lower value of V_{OC} due to much lower LUMO energy levels in the absence of a vinyl linker in the acceptor unit. Based on the predicted V_{OC} , it is anticipated that a blend of PBDB-T-SF donor and methoxy functionalized acceptor would yield an improved OSC performance. However, one must be cautious about the other parameters, such as J_{SC} , governing the PCE of an OSC. As demonstrated by Markina *et al.*,²⁸ it is often observed that V_{OC} and J_{SC} follow a contrasting order, making the overall process of optimizing the NFA-donor combination a complex problem to solve. To address this, in the following section, we have analyzed quadrupole moments in these NFAs.

Quadrupole moment

The quadrupole moment of acceptor molecules plays a crucial role in the interfacial energetics in NFA-based organic solar cells.²⁷

In an A–D–A type molecular architecture, the presence of stronger acceptors (strong electron-withdrawing moieties) results in a reduced HOMO–LUMO gap in the molecule. However, for the same reason, there is a net increase in the charge flow within the molecule, leading to a more significant molecular quadrupole moment.²⁸ It was previously shown that the larger quadrupole moment of the acceptor results in efficient dissociation of the charge transfer (CT) state in bulk heterojunction donor–NFA based blends.²⁹ Consequently, there is an overall improvement in the internal quantum efficiency (IQE), J_{SC} , and fill factor of the device. However, a significant quadrupole moment also comes up with a negative impact on the V_{OC} . Strong electron-withdrawing groups resulted in increased electron affinities and reduced IE–EA gap, reducing the interfacial CT state energy and yielding lower V_{OC} of the device. We have computed the quadrupole moment perpendicular to the π -system (Q_{20}) for all studied NFAs and correlated it with the V_{OC} values obtained against the PBDB-T donor, as shown in Fig. 5. Since the computed V_{OC} values overestimated the experimental measurements, we estimated a correction factor based on the average deviation between the experimental and predicted values, as summarized in Tables S2 and S3 of the ESI.† The correction term (0.4 eV) was then subtracted from the calculated numbers, and the x -axis in 5 exhibits the same quantity. As anticipated, we observed an inverse correlation between V_{OC} and Q_{20} . Most importantly, this correlation holds for different donor molecules considered in our study. We could not show a direct correlation between J_{SC} and Q_{20} since it is highly challenging to obtain the former quantity computationally. However, as suggested by Markina *et al.*,²⁸ the trade-off between gain in J_{SC} and V_{OC} loss can be optimized by designing acceptor molecules with quadrupole moment values ~ 100 ea_0^2 . The J_{SC} values of the experimentally reported NFAs are summarized in Table S3 of the ESI.† Among the experimentally reported NFAs, we found that the four NFAs, such as IT-H, IT-F, ITIC-Th-3, and IT-OMe-2, exhibit $J_{SC} > 17$ mA cm^{-2}

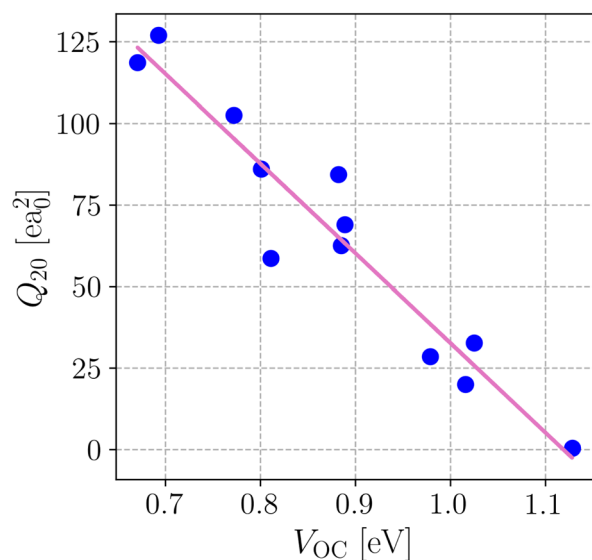


Fig. 5 Quadrupole moment perpendicular to the π -system (Q_{20}) against the V_{OC} obtained for PBDB-T donor–NFA-based blends.

and have molecular quadrupole moments in the range of 80 to 130 ea_0^2 . In addition, we observed that four of the designed NFAs (SeTIC-F, SeTIC-Cl, ITIC-Th-1, and ITIC-Th-2) have quadrupole moments > 80 ea_0^2 which may result in sizeable J_{SC} and they may act as promising candidates for efficient OSCs.

The computed Q_{20} values were also compared against each compound's highest and lowest occupied molecular orbitals (HOMO and LUMO), as shown in Fig. 6. It is evident from Fig. 6 that a larger HOMO–LUMO gap yields a smaller Q_{20} . Among the experimentally studied blends, PBDB-T-SF:IT-H, PBDB-T:IT-OMe-2, PBDB-T-SF:IT-4F, and FTAZ:ITIC-Th-3 showed relatively high PCE values of 11.05, 11.9, 13.1, and 12.1, respectively.^{8,62,63} These acceptor molecules possess Q_{20} in the range 65–120 ea_0^2 in combination with a low HOMO–LUMO gap (< 2.1 eV). Although based on a small set of samples, the observed trend indicates that the fluorinated SeTIC derivatives possessing the smallest HOMO–LUMO differences (< 1.1 eV) and Q_{20} value of 80.32 and 87.67 ea_0^2 , respectively, may act as a promising acceptor for the bulk heterojunction OSCs. Moreover, these acceptors exhibit the largest λ_{max} in the near-infrared region that can serve as complementary absorption to donor photon absorption in the middle of the visible region, eventually leading to an efficient photon harvesting blend. Along similar lines, in the Type-2 compounds, both ITIC-Th-1 and ITIC-Th-2 are promising potential NFA acceptors with 80 $ea_0^2 < Q_{20} < 100$ ea_0^2 , in contrast to ITIC-Th-4 possessing $Q_{20} \sim 55$ ea_0^2 .

Transition density matrix

The transition density matrix (TDM) representation helps describe the intra-molecular interaction between donors and acceptors of the π -conjugated system by defining a 2D-color code-mapped plot of their electronic densities.⁶⁷ The TDMs were computed at the B3LYP/6-31+G(d,p) level of theory by evaluating the emission and absorption spectra of the S1 state, considering chloroform as the solvent. In the TDM analysis, the investigated NFAs are divided into two categories concerning the number of atoms present in the donor (D) and acceptor

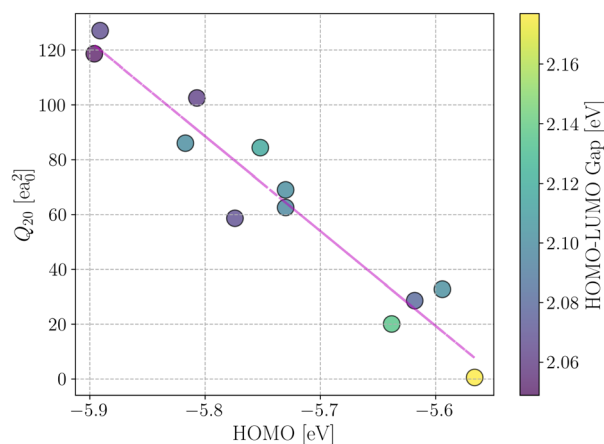


Fig. 6 Q_{20} -HOMO correlation plot for the investigated NFA complexes. The color of each point represents the corresponding HOMO–LUMO gap value.

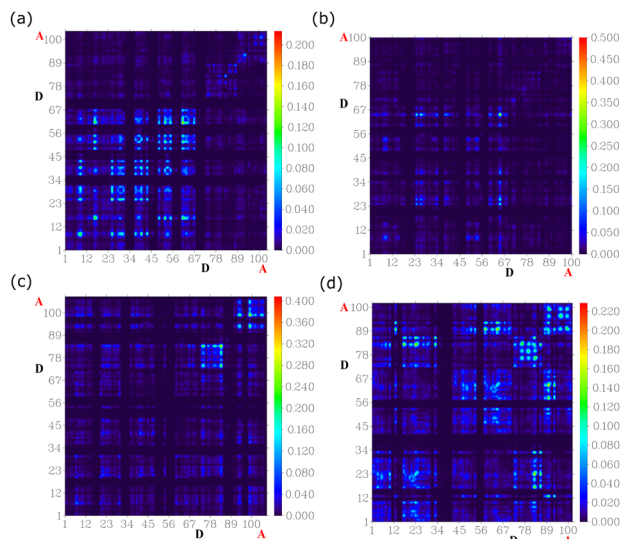


Fig. 7 Graphical representation of the transition density matrix (TDM) at the S1 state of selected non-fullerene acceptors: (a) IT-H, (b) ITIC-Th, (c) IT-OMe-1, and (d) SeTIC. These are generated with the help of Multiwfn 3.7 software.⁶⁰ Similar plots for the remaining compounds are shown in Fig. S6 of the ESI.†

(A) units. The hydrogen atoms are neglected due to their negligible contribution compared to the total unit. The 2D-color-mapped TDMs of a few NFAs are shown in Fig. 7, whereas the remaining system is depicted in Fig. S6 of the ESI.† The TDM graphs demonstrate an apparent diagonal charge coherence from donor to acceptor for all the investigated NFAs. However, the maximum diagonal charge coherence is found in SeTIC, IT-OMe-1, and IT-H compared to ITIC-Th (Fig. 7), which suggests that the transfer of electron density is more significant from the donor toward the acceptor unit. Furthermore, more intense diagonal charge coherence is observed in -F and -Cl substituted NFAs (Fig. S6, ESI†), which suggested that the end-capped acceptor units can easily draw electron density from the core unit. The core unit of the NFAs has electron-rich atoms that may efficiently donate electron density. The alternate substitution of -F, and -OMe groups at the X, Y, Z, and T positions of ITIC-Th and IT-OMe NFAs have measured a negligible effect on their 2D-color code-mapped plot. Besides, the more intense off-diagonal fringes indicate the significant charge transfer in the SeTIC derivatives.

In addition, we have also explored the effects of tailoring the side chains from hexyl to methyl and its subsequent impact on the photovoltaic characteristics and optoelectronic properties of the NFAs. We noticed that side-chain engineering does not significantly influence the NFA systems' overall photovoltaic and optoelectronic properties. A minor change (0.06–0.089 eV) in the HOMO–LUMO gap and V_{OC} between the two side chains incorporated in IT-H, ITIC-Th, and IT-OMe-3 is observed. Based on these observations, we may conclude that from the experimental point of view, it is not harmful to engineer the side chains (increase) of NFAs to achieve better solubility and slightly improved performance. In contrast, for the computational study, tailoring the side chain (reduce) helps to reduce the overall

computational cost without affecting the performance of the OSCs.

4. Conclusions

This work employed an electronic structure framework to study the optoelectronic and photovoltaic properties of three types of acceptor–donor–acceptor-based non-fullerene acceptor molecules for organic solar cell applications. Our goal was to investigate the role of functionalization in the acceptor unit by incorporating electron-withdrawing groups, such as fluorine, chlorine, and methoxy, on the overall performance of the NFA systems. Structural analysis *via* the torsional angles connecting the donor and acceptor units revealed that all the Type-1 and Type-2 NFAs are planar with the most significant deviation of 5.5 from planarity. Due to the absence of vinyl linkers between the donor and acceptor motifs, the SeTIC derivatives, Type-3 NFAs, exhibited nonplanar geometry with twisting angles around 17. Therefore, the vinyl linker plays a significant role in obtaining a planar and rigid NFA backbone. The presence of the electron-withdrawing groups, such as halogen atoms and -OMe group, in the acceptor part of the NFAs, revealed contrasting effects on the gas-phase energy levels, ionization energy, and electron affinities. In the case of halogen functionalization, the IP and EA values increased up to 0.23 eV (compared to the parent system), whereas their magnitudes were reduced up to 0.21 eV in the presence of -OMe. On a similar note, tailoring the electronegativity of the acceptor exhibited a significant impact on the computed HOMO–LUMO gaps in the investigated systems. The calculated HOMO–LUMO gaps in the Type-1 and Type-2 systems were comparable, around ~ 2 eV, whereas the SeTIC derivatives showed a shallower band gap of around 1.02 eV. The inclusion of the -OMe (halogen) group resulted in an enhanced (reduced) LUMO energy which was also reflected in the corresponding improved V_{OC} values. The predicted absorption maximum showed satisfactory agreement with the available experimental measurements. Overall we observed red-shifted λ_{max} upon halogen functionalization, whereas the acquisition of -OMe groups led to a blue shift in the λ_{max} . All the investigated systems showed absorption in the UV-visible region except for the SeTIC derivatives, which possess λ_{max} in the near-infrared part of wavelength 1060–1090 nm. The presence of such a sizeable bathochromic shift in λ_{max} indicates that these SeTIC-based molecules can serve as complementary to donor photon absorption, ultimately guiding to an efficient photon harvesting mixture. Therefore, the replacement of sulfur atoms by selenium atoms in the core part and, concomitantly, appropriate tuning of the electron-withdrawing groups in the acceptor fragment should be an essential guide while designing the next generation NFAs.

Four different donor polymers, such as PBDB-T, PBDB-T-SF, PM6, and FTAZ, were considered to predict V_{OC} using eqn (2). Although the computed V_{OC} consistently overestimated the experimental values, the trend observed in the V_{OC} was the

same as in the experiment. Among the polymers investigated, PBDB-T-SF performed the best based on the highest V_{OC} values obtained in combination with any of the examined NFA molecules. Due to the lowering of the LUMO levels in the halogen-functionalized systems, the V_{OC} values were found to be degraded, in contrast to -OMe functionalization. Among all the NFAs, the SeTIC derivatives showed minimum V_{OC} . However, the computed exciton binding energy in the SeTIC-based systems was lowest due to the small HOMO–LUMO gap. A smaller exciton binding energy is anticipated to facilitate a spontaneous dissociation of the exciton, rendering separated charge carriers and an enhanced J_{SC} and fill factor of the OSC. Furthermore, the correlation between Q_{20} and V_{OC} or J_{SC} indicated that the loss in V_{OC} and gain in J_{SC} can be optimized by designing NFAs with a quadrupole moment in the range 80 to 130 ea_0^2 , a similar range to that reported earlier by Markina *et al.*²⁸ Therefore, to address the trade-off between V_{OC} and J_{SC} , and optimize the performance in terms of improved absorption and high V_{OC} and J_{SC} , it is essential to concentrate on both core and terminal group modifications. In this regard, four of the designed NFA molecules, SeTIC-F, SeTIC-Cl, ITIC-Th-1, and ITIC-Th-2, revealed Q_{20} in the range as mentioned above, along with red-shifted absorption maximum and very high oscillator strength. These NFAs could act as a potential non-fullerene acceptor in bulk-heterojunction OSCs.

In summary, A–D–A-based non-fullerene acceptors exhibit tremendous potential as active materials in organic solar cells. Although significant progress is being made in this field, a large window of opportunity exists to adjust the microscopic details within the NFA building blocks and achieve improved solar cell performance. The design criteria must focus on a small HOMO–LUMO gap, enhanced LUMO energy, and, consequently, a considerable value of Q_{20} in the range of 80 to 130 ea_0^2 . We can navigate the optical and fundamental band gap in a targeted region by carefully selecting the electronegative groups and replacing sulfur atoms with selenium atoms. Furthermore, to better understand the hole–electron transport and exciton dynamics in these NFA systems, bulk morphology simulations followed by charge transport calculations are required. These constitute our future set of objectives.

Author contributions

AM devised the problem. BD and RK performed all the simulations. AM, BD, and RK analyzed the results and prepared the draft.

Conflicts of interest

There are no conflicts to declare.

Acknowledgements

The authors gratefully acknowledge the Indian Institute of Technology Gandhinagar, India, for providing the research facilities and support. AM acknowledges the SERB (SRG/2022/

001532) project for funding. We also thank Prof. Biswajit Mondal for the critical reading of the manuscript and fruitful discussions.

References

- 1 P. Meredith, W. Li and A. Armin, *Adv. Energy Mater.*, 2020, **10**, 2001788.
- 2 A. Armin, W. Li, O. J. Sandberg, Z. Xiao, L. Ding, J. Nelson, D. Neher, K. Vandewal, S. Shoaee, T. Wang, H. Ade, T. Heumüller, C. Brabec and P. Meredith, *Adv. Energy Mater.*, 2021, **11**, 2003570.
- 3 Y. Cui, H. Yao, J. Zhang, T. Zhang, Y. Wang, L. Hong, K. Xian, B. Xu, S. Zhang, J. Peng, Z. Wei, F. Gao and J. Hou, *Nat. Commun.*, 2019, **10**, 2515.
- 4 J. Yuan, Y. Zhang, L. Zhou, G. Zhang, H.-L. Yip, T.-K. Lau, X. Lu, C. Zhu, H. Peng, P. A. Johnson, M. Leclerc, Y. Cao, J. Ulanski, Y. Li and Y. Zou, *Joule*, 2019, **3**, 1140–1151.
- 5 Y. Lin, B. Adilbekova, Y. Firdaus, E. Yengel, H. Faber, M. Sajjad, X. Zheng, E. Yarali, A. Seitkhan, O. M. Bakr, A. El-Labban, U. Schwingenschlögl, V. Tung, I. McCulloch, F. Laquai and T. D. Anthopoulos, *Adv. Mater.*, 2019, **31**, 1902965.
- 6 Q. Liu, Y. Jiang, K. Jin, J. Qin, J. Xu, W. Li, J. Xiong, J. Liu, Z. Xiao, K. Sun, S. Yang, X. Zhang and L. Ding, *Sci. Bull.*, 2020, **65**, 272–275.
- 7 J. Zhao, Y. Li, G. Yang, K. Jiang, H. Lin, H. Ade, W. Ma and H. Yan, *Nat. Energy*, 2016, **1**, 15027.
- 8 S. Li, L. Ye, W. Zhao, S. Zhang, H. Ade and J. Hou, *Adv. Energy Mater.*, 2017, **7**, 1700183.
- 9 S. Li, W. Liu, C.-Z. Li, M. Shi and H. Chen, *Small*, 2017, **13**, 1701120.
- 10 J. Zhang, W. Liu, S. Chen, S. Xu, C. Yang and X. Zhu, *J. Mater. Chem. A*, 2018, **6**, 22519–22525.
- 11 P. Cheng, G. Li, X. Zhan and Y. Yang, *Nat. Photonics*, 2018, **12**, 131–142.
- 12 J. Hou, O. Inganäs, R. H. Friend and F. Gao, *Nat. Mater.*, 2018, **17**, 119–128.
- 13 C. Yan, S. Barlow, Z. Wang, H. Yan, A. K.-Y. Jen, S. R. Marder and X. Zhan, *Nat. Rev. Mater.*, 2018, **3**, 18003.
- 14 M. A. Green, Y. Hishikawa, E. D. Dunlop, D. H. Levi, J. Hohl-Ebinger and A. W. Ho-Baillie, *Prog. Photovolt.: Res. Appl.*, 2018, **26**, 3–12.
- 15 A. Tang, W. Song, B. Xiao, J. Guo, J. Min, Z. Ge, J. Zhang, Z. Wei and E. Zhou, *Chem. Mater.*, 2019, **31**, 3941–3947.
- 16 Y. Xu, H. Yao, L. Ma, J. Wang and J. Hou, *Rep. Prog. Phys.*, 2020, **83**, 082601.
- 17 W. Gao, M. Zhang, T. Liu, R. Ming, Q. An, K. Wu, D. Xie, Z. Luo, C. Zhong, F. Liu, F. Zhang, H. Yan and C. Yang, *Adv. Mater.*, 2018, **30**, 1800052.
- 18 B. Kan, X. Chen, K. Gao, M. Zhang, F. Lin, X. Peng, F. Liu and A. K.-Y. Jen, *Nano Energy*, 2020, **67**, 104209.
- 19 W. Wang, P. Shen, X. Dong, C. Weng, G. Wang, H. Bin, J. Zhang, Z.-G. Zhang and Y. Li, *ACS Appl. Mater. Interfaces*, 2017, **9**, 4614–4625.

- 20 Y. Li, J.-D. Lin, X. Che, Y. Qu, F. Liu, L.-S. Liao and S. R. Forrest, *J. Am. Chem. Soc.*, 2017, **139**, 17114–17119.
- 21 X. Jia, G. Liu, S. Chen, Z. Li, Z. Wang, Q. Yin, H.-L. Yip, C. Yang, C. Duan, F. Huang and Y. Cao, *ACS Appl. Energy Mater.*, 2019, **2**, 7572–7583.
- 22 D. Su, M.-A. Pan, Z. Liu, T.-K. Lau, X. Li, F. Shen, S. Huo, X. Lu, A. Xu, H. Yan and C. Zhan, *Chem. Mater.*, 2019, **31**, 8908–8917.
- 23 G. Liu, T. Jia, K. Zhang, J. Jia, Q. Yin, W. Zhong, X. Jia, N. Zheng, L. Ying, F. Huang and Y. Cao, *Chem. Mater.*, 2020, **32**, 1022–1030.
- 24 A.-J. Payne, S. Li, S. V. Dayneko, C. Risko and G. C. Welch, *Chem. Commun.*, 2017, **53**, 10168–10171.
- 25 H. Bin, L. Gao, Z.-G. Zhang, Y. Yang, Y. Zhang, C. Zhang, S. Chen, L. Xue, C. Yang, M. Xiao and Y. Li, *Nat. Commun.*, 2016, **7**, 13651.
- 26 D. Qian, Z. Zheng, H. Yao, W. Tress, T. R. Hopper, S. Chen, S. Li, J. Liu, S. Chen, J. Zhang, X.-K. Liu, B. Gao, L. Ouyang, Y. Jin, G. Pozina, I. A. Buyanova, W. M. Chen, O. Inganäs, V. Coropceanu, J.-L. Bredas, H. Yan, J. Hou, F. Zhang, A. A. Bakulin and F. Gao, *Nat. Mater.*, 2018, **17**, 703–709.
- 27 S. Karuthedath, J. Gorenflot, Y. Firdaus, N. Chaturvedi, C. S. P. De Castro, G. T. Harrison, J. I. Khan, A. Markina, A. H. Balawi, T. A. D. Peña, W. Liu, R.-Z. Liang, A. Sharma, S. H. K. Paleti, W. Zhang, Y. Lin, E. Alarousu, S. Lopatin, D. H. Anjum, P. M. Beaujuge, S. De Wolf, I. McCulloch, T. D. Anthopoulos, D. Baran, D. Andrienko and F. Laquai, *Nat. Mater.*, 2021, **20**, 378–384.
- 28 A. Markina, K.-H. Lin, W. Liu, C. Poelking, Y. Firdaus, D. R. Villalva, J. I. Khan, S. H. K. Paleti, G. T. Harrison, J. Gorenflot, W. Zhang, S. De Wolf, I. McCulloch, T. D. Anthopoulos, D. Baran, F. Laquai and D. Andrienko, *Adv. Energy Mater.*, 2021, **11**, 2102363.
- 29 J. I. Khan, M. A. Alamoudi, N. Chaturvedi, R. S. Ashraf, M. N. Nabi, A. Markina, W. Liu, T. A. Dela Peña, W. Zhang, O. Alévêque, G. T. Harrison, W. Alsufyani, E. Levillain, S. De Wolf, D. Andrienko, I. McCulloch and F. Laquai, *Adv. Energy Mater.*, 2021, **11**, 2100839.
- 30 A. Wadsworth, H. Bristow, Z. Hamid, M. Babics, N. Gasparini, C. W. Boyle, W. Zhang, Y. Dong, K. J. Thorley, M. Neophytou, R. S. Ashraf, J. R. Durrant, D. Baran and I. McCulloch, *Adv. Funct. Mater.*, 2019, **29**, 1808429.
- 31 M. Chen, D. Liu, W. Li, R. S. Gurney, D. Li, J. Cai, E. L. K. Spooner, R. C. Kilbride, J. D. McGettrick, T. M. Watson, Z. Li, R. A. L. Jones, D. G. Lidzey and T. Wang, *ACS Appl. Mater. Interfaces*, 2019, **11**, 26194–26203.
- 32 X. Du, T. Heumueller, W. Gruber, A. Classen, T. Unruh, N. Li and C. J. Brabec, *Joule*, 2019, **3**, 215–226.
- 33 Y. Zhang, Y. Wang, T. Shan and H. Zhong, *ACS Appl. Energy Mater.*, 2022, **5**, 11283–11291.
- 34 H. Cao, N. Bauer, C. Pang, J. Rech, W. You and P. A. Rugar, *ACS Appl. Energy Mater.*, 2018, **1**, 7146–7152.
- 35 K. Xian, Y. Cui, Y. Xu, T. Zhang, L. Hong, H. Yao, C. An and J. Hou, *J. Phys. Chem. C*, 2020, **124**, 7691–7698.
- 36 Y. Wang, Y. Zhang, N. Qiu, H. Feng, H. Gao, B. Kan, Y. Ma, C. Li, X. Wan and Y. Chen, *Adv. Energy Mater.*, 2018, **8**, 1702870.
- 37 X. Li, J. Yao, I. Angunawela, C. Sun, L. Xue, A. Liebman-Pelaez, C. Zhu, C. Yang, Z.-G. Zhang and H. Ade, *et al.*, *Adv. Energy Mater.*, 2018, **8**, 1800815.
- 38 G. Kuppang, X. Chen and J. Brédas, *Mater. Today Adv.*, 2021, **11**, 100154.
- 39 L. Benatto, C. A. M. Moraes, G. Candiotti, K. R. A. Sousa, J. P. A. Souza, L. S. Roman and M. Koehler, *J. Mater. Chem. A*, 2021, **9**, 27568–27585.
- 40 W. Qiu and S. Zheng, *Sol. RRL*, 2021, **5**, 2100023.
- 41 S. Haseena, M. Jyothirmai and M. Kumar Ravva, *Sol. Energy*, 2022, **242**, 201–211.
- 42 M. Andrea, K. Kordos, E. Lidorikis and D. Papageorgiou, *Comput. Mater. Sci.*, 2022, **202**, 110978.
- 43 J. Liu, Z. Li, J. Wang, X. Zhang, X. Zhan and G. Lu, *J. Mater. Chem. A*, 2020, **8**, 23304–23312.
- 44 G. Zhang, X.-K. Chen, J. Xiao, P. C. Y. Chow, M. Ren, G. Kuppang, X. Jiao, C. C. S. Chan, X. Du, R. Xia, Z. Chen, J. Yuan, Y. Zhang, S. Zhang, Y. Liu, Y. Zou, H. Yan, K. S. Wong, V. Coropceanu, N. Li, C. J. Brabec, J.-L. Bredas, H.-L. Yip and Y. Cao, *Nat. Commun.*, 2020, **11**, 3943.
- 45 G. Han, Y. Guo, X. Song, Y. Wang and Y. Yi, *J. Mater. Chem. C*, 2017, **5**, 4852–4857.
- 46 G. Han, Y. Guo, L. Ning and Y. Yi, *Sol. RRL*, 2019, **3**, 1800251.
- 47 J. Yang, W.-L. Ding, Q.-S. Li and Z.-S. Li, *J. Phys. Chem. Lett.*, 2022, **13**, 916–922.
- 48 C. Yao, Y. Yang, L. Li, M. Bo, J. Zhang, C. Peng, Z. Huang and J. Wang, *J. Phys. Chem. C*, 2020, **124**, 23059–23068.
- 49 J. Yang, Q.-S. Li and Z.-S. Li, *Phys. Chem. Chem. Phys.*, 2021, **23**, 12321–12328.
- 50 M. J. Frisc *et al.*, *Gaussian 09 Revision E.01*, Gaussian Inc. Wallingford CT, 2009.
- 51 R. Dennington, T. A. Keith and J. M. Millam, *GaussView Version 6*, Semichem Inc. Shawnee Mission KS, 2019.
- 52 B. Civalleri, C. M. Zicovich-Wilson, L. Valenzano and P. Ugliengo, *CrystEngComm*, 2008, **10**, 405–410.
- 53 M. I. Khan, J. Iqbal, S. J. Akram, Y. A. El-Badry, M. Yaseen and R. A. Khera, *J. Mol. Graphics Modell.*, 2022, **113**, 108162.
- 54 V. Rühle, A. Lukyanov, F. May, M. Schrader, T. Vehoff, J. Kirkpatrick, B. Baumeier and D. Andrienko, *J. Chem. Theory Comput.*, 2011, **7**, 3335–3345.
- 55 A. J. Stone, *J. Chem. Theory Comput.*, 2005, **1**, 1128–1132.
- 56 E. Runge and E. K. U. Gross, *Phys. Rev. Lett.*, 1984, **52**, 997–1000.
- 57 V. Barone and M. Cossi, *J. Phys. Chem. A*, 1998, **102**, 1995–2001.
- 58 M. Irfan, J. Iqbal, S. Sadaf, B. Eliasson, U. A. Rana, S. Ud-din Khan and K. Ayub, *Int. J. Quantum Chem.*, 2017, **117**, e25363.
- 59 M. C. Scharber, D. Mühlbacher, M. Koppe, P. Denk, C. Waldauf, A. J. Heeger and C. J. Brabec, *Adv. Mater.*, 2006, **18**, 789–794.
- 60 T. Lu and F. Chen, *J. Comput. Chem.*, 2012, **33**, 580–592.
- 61 W. Humphrey, A. Dalke and K. Schulten, *J. Mol. Graphics*, 1996, **14**, 33–38.
- 62 W. Zhao, S. Li, H. Yao, S. Zhang, Y. Zhang, B. Yang and J. Hou, *J. Am. Chem. Soc.*, 2017, **139**, 7148–7151.

- 63 F. Zhao, S. Dai, Y. Wu, Q. Zhang, J. Wang, L. Jiang, Q. Ling, Z. Wei, W. Ma and W. You, *et al.*, *Adv. Mater.*, 2017, **29**, 1700144.
- 64 S. Li, L. Ye, W. Zhao, S. Zhang, H. Ade and J. Hou, *Adv. Energy Mater.*, 2017, **7**, 1700183.
- 65 M. Khalid, M. U. Khan, S. Ahmed, Z. Shafiq, M. M. Alam, M. Imran, A. A. C. Braga and M. S. Akram, *Sci. Rep.*, 2021, **11**, 1–15.
- 66 C. Yang, S. Zhang, J. Ren, M. Gao, P. Bi, L. Ye and J. Hou, *Energy Environ. Sci.*, 2020, **13**, 2864–2869.
- 67 S. Tretiak and S. Mukamel, *Chem. Rev.*, 2002, **102**, 3171–3212.